AIAA JOURNAL
Vol. 50, No. 6, June 2012

Numerical Investigation of Hypersonic Boundary-Layer Stabilization by Porous Surfaces

Viola Wartemann* and Heinrich Lüdeke†
DLR, German Aerospace Center, 38108 Braunschweig, Germany
and
Neil D. Sandham‡
University of Southampton, Southampton, England SO17 1BJ, United Kingdom

DOI: 10.2514/1.J051355

The acoustic second-mode instability predicted by linear stability theory is compared with direct numerical simulation for a hypersonic flow over various porous walls. The damping effect of the micropores on the second mode is shown by comparison of the two different approaches. In addition to investigating the effect of pore size, the influence of the pore shape is studied by using spanwise grooves and cylindrical pores. Specifically, the comparability of different pore shapes by two definitions of hydraulic diameter is analyzed. The influence of rarefied gas behavior of the flow inside the pores is also investigated by comparing a slip boundary condition with finite Knudsen numbers with a nonslip boundary condition for different radii and pore depths.

Nomenclature

A	=	admittance; area
B	=	thermal admittance
b	=	groove half-width
C	=	pore circumference
c	=	stretching factor
$\bar{c}$	=	mean molecular velocity
d	=	pore depth
d_h	=	hydraulic diameter
J_0, J_1	=	Bessel functions of the first kind
Kn	=	Knudsen number
$L_{x,y,z}$	=	plate dimensions
M	=	Mach number
n	=	porosity
n_p	=	number of pores/grooves per wavelength
Pr	=	Prandtl number
q	=	flow/material quantity
R	=	gas constant
r	=	pore radius
S	=	surface
T	=	temperature
t	=	time
u, v, w	=	velocity in x-, y-, and z-directions
V	=	volume
w	=	groove width
x, y, z	=	coordinates
Z_0	=	characteristic impedance
α, β	=	wave numbers
$-\alpha_i$	=	spatial growth rate
γ	=	ratio of specific heats
δ^*	=	displacement thickness
η_m	=	coordinate of pore bottom
κ	=	thermal conductivity
Λ	=	propagation constant
μ	=	nondimensional wall-normal coordinate; viscosity
ϱ	=	density
ω	=	frequency
ω_i	=	temporal growth rate

Indices

i	=	imaginary part
l	=	limit value
p	=	pore
r	=	real part
w	=	wall quantity

Superscripts

$\bar{}$	=	base flow quantity
$\tilde{}$	=	disturbance flow quantity
$\hat{}$	=	eigenfunction

I. Introduction

HYPERSONIC laminar flow control for delayed laminar-turbulent transition is of high importance for reentry vehicles because early transition results in an increase in the heat transfer by factors between 3 and 8, resulting in a cost and weight increase of thermal protection systems [1,2]. A lot of different strategies are used to delay or prevent the transition process. Classical flow-control strategy began with natural laminar flow, which has been applied since the 1930s and implies delaying transition by modifying the body shape. By contrast, active laminar flow control (LFC), which started around the same time, uses suction or wall cooling/heating to influence the boundary-layer instability modes [3]. In the present work, the manipulation of the transition is performed in a passive way, which usually provides a lower cost compared with active systems. Also, the hypersonic environmental conditions make the use of active LFC more difficult than in other flight regimes.

In this paper, the manipulation of the transition is performed by the use of porous surfaces to influence the growth of the second mode. The second mode, or so-called Mack mode [4], is the dominant mode for the transition process at hypersonic Mach numbers.

In an early work, Fedorov et al. [5] have theoretically shown, by linear stability theory (LST), a strong stabilization effect of the second mode by a passive porous surface, which partially dissipates disturbance energy inside the pores. Using an analytical model of flow within blind, thin pores, typically with about 10–20 pores per wavelength of the Mack modes and a porosity about 25%, the growth

Received 20 April 2011; revision received 9 December 2011; accepted for publication 10 December 2011.

*Ph.D.; viola.wartemann@dlr.de (Corresponding Author).
†Research Scientist; heinrich.luedeke@dlr.de.
‡Professor, School of Engineering Sciences; n.sandham@soton.ac.uk. Senior Member AIAA.

rate reduction is predicted to be a factor of 2 [5]. Experiments of Rasheed et al. [6] on a 5 deg half-angle sharp cone ($M_\infty \sim 5$–6) fitted with micropores confirmed the theoretical prediction. Continuation activities, theoretical as well as experimental, around the working group of Fedorov have demonstrated robustness of this laminar flow control concept [7–16]. Direct numerical simulation (DNS) confirmed the results of the LST; Egorov et al. [17] carried out the first two-dimensional (2-D) DNS using, as a theoretical model, the porous surface boundary conditions formulation of Federov et al. [5,8,9]. Bres et al. [18–20], Lüdeke et al. [21], Wartemann et al. [22], and Wartemann and Lüdeke [23] have shown 2-D simulations with resolved pores. A study of the effect by DNS with a three-dimensional pore flow was first presented by Sandham and Lüdeke [24]. The final breakdown to turbulence was studied in De Tullio and Sandham [25], showing that the stabilizing effect of passive porous walls continues for the nonlinear stages of transition.

In this paper, two simulation techniques are used; DNS, by a fourth-order finite difference version of the DLR FLOWer code, which is used to provide full Navier–Stokes solutions of the boundary-layer flow over the surface as well as inside the pores, was compared with two different linear stability codes: the spatial DLR nonlocal transition analysis (NOLOT) code and the spatial/temporal linear stability code of the University of the Southampton (SLST). Detailed investigations show good agreement between the two different approaches [22,23]. The actual calculations show the influence of pore shape using cylindrical pores and spanwise grooves (Section III). In particular, the accuracy of two different defined hydraulic diameters is studied.

Section IV of the present paper investigates the influence of rarefied gases inside the pores modeled by slip boundary conditions at finite Knudsen number Kn, which is the ratio of characteristic length scales. As shown by Maslov et al. [7], the flow inside the pores cannot always be treated as a continuum because the mean free path of the fluid particles inside the cavities has a significant value in comparison with the microscopic pore diameter, so generally the Knudsen number, based on this diameter, is no longer small. Within the present study, the influence of the slip boundary condition at different Knudsen numbers in comparison with the nonslip boundary condition calculated by DNS and LST is shown.

Overall, good agreement of both methods (LST and DNS) is demonstrated for a Mach 6 boundary layer flow over different porous walls.

II. Numerical Methods

A. Linear Stability Theory

1. NOLOT

The NOLOT code [26], which is a spatial linear stability code, was developed in cooperation between DLR and Swedish Defence Research Agency and can be used for local as well as nonlocal analyses. In this work, the local linear spatial approach is used, which is a subset of the nonlocal stability equations. The equations are derived from the equations of conservation of mass, momentum, and energy, which govern the flow of a viscous, compressible, ideal gas, formulated in primitive variables. All dimensions of this section are normalized with the displacement thickness δ^*, whereas the dimensionless flow quantities are normalized by the values at the boundary layer edge. The flow and material quantities are decomposed into a steady laminar basic flow $\bar{q}$ and an unsteady disturbance flow $\tilde{q}$

$$q(x, y, z, t) = \bar{q}(x, y) + \tilde{q}(x, y, z, t) \tag{1}$$

The disturbance $\tilde{q}$ is represented as a harmonic wave

$$\tilde{q}(x, y, z, t) = \hat{q}(x, y) \exp[i(\alpha x + \beta z - \omega t)] \tag{2}$$

with the complex-valued amplitude function $\hat{q}$. In the following expression, the hat over a variable denotes an amplitude function. Because NOLOT is a spatial code, the wavenumbers α and β are complex quantities, and the frequency ω is a real value. $-\alpha_i$ is the spatial growth rate, which is the quantity of primary interest. The boundary conditions in NOLOT for a smooth wall (at $y = 0$) are

$$\hat{u}_w, \hat{v}_w, \hat{w}_w, \hat{T}_w = 0 \tag{3}$$

The NOLOT code is validated with the help of several test cases against published results, including DNS, parabolized stability equations, multiple scales methods, and LST. A good summary of the validation is given by Hein et al. [26]. For the treatment of porous surfaces with nonslip and slip walls inside the pores, additional boundary conditions were implemented. The validation of the nonslip boundary condition and of the slip boundary condition is given in Wartemann et al. [22] and Wartemann and Lüdeke [23], respectively. Boundary conditions for porous walls are taken from Maslov et al. [7] and Koslov et al. [27]; a complete derivation can be found in these references. They are given by

$$\hat{u}_w, \hat{w}_w = 0, \qquad \hat{v}_w = A\hat{p}_w, \qquad \hat{T}_w = B\hat{p}_w \tag{4}$$

where a subscript w denotes the value at the wall. Section III.B of this work shows that the thermal admittance B has a marginal effect ($<0.5\%$), which is also described in Fedorov et al. [5]. It is consequently neglected in the rest of the present work. The admittance A is calculated by

$$A = \frac{n}{Z_0}\tanh(md) \tag{5}$$

The investigated pores are equally spaced, blind pores with a depth d and the porosity n. The characteristic impedance Z_0 and the propagation constant m are

$$Z_0 = -\frac{\sqrt{\frac{\hat{\rho}}{\hat{C}}}}{M\sqrt{T_w}}, \quad m = \frac{i\omega M\sqrt{\hat{\rho}\,\hat{C}}}{\sqrt{T_w}} \tag{6}$$

where the dimensionless complex dynamic density $\hat{\rho}$ and dynamic compressibility $\hat{C}$ are expressed as

$$\hat{\rho} = \frac{1}{1 - F(B_u, \Lambda)}, \qquad \hat{C} = 1 + (\gamma - 1)F(B_E, \hat{\Lambda}) \tag{7}$$

The function F and the propagation constant Λ depend on the pore shape. In this study, two different pore shapes for the formulations inside the NOLOT code are used: cylindrical pores:

$$F(\Lambda) = \frac{2J_1(\Lambda)}{\Lambda J_0(\Lambda)} \tag{8}$$

where J_0 and J_1 are Bessel functions of the argument Λ and $\hat{\Lambda}$, where

$$\Lambda = r\sqrt{\frac{i\omega\rho_0}{\mu}}, \qquad \hat{\Lambda} = \Lambda\sqrt{Pr} \tag{9}$$

and spanwise grooves:

$$F(\Lambda) = \frac{\tan\Lambda}{\Lambda} \tag{10}$$

with

$$\Lambda = b\sqrt{\frac{i\omega\rho_0}{\mu}}, \qquad \hat{\Lambda} = \Lambda\sqrt{Pr} \tag{11}$$

where r is the pore radius, and b the spanwise groove half-width. ω represents the dimensionless angular frequency.

Because of the fact that, inside pores with a small radius r, the mean free path λ of the molecules becomes comparable to the relevant length scales of the shear layer, the flow cannot always be treated by a continuum approach [7]. By using a slip boundary condition, the function F depends on additional factors, as shown

in the following equations for the spanwise grooves boundary condition:

$$F(A_u, Kn, \Lambda) = \frac{\tan\Lambda}{\Lambda[1 - KnA_u\Lambda\tan\Lambda]} \tag{12}$$

The Knudsen number is defined as

$$Kn = \frac{4\mu}{\rho\bar{c}b} \tag{13}$$

where μ is the dynamic viscosity, ρ is the density, $\bar{c} = \sqrt{8RT/\pi}$ is the mean molecular velocity with the gas constant R, and T is the gas temperature. The dimensionless factors A_u and A_e are outcomes of the gas kinetic theory. They are a measure of the interaction of gas molecules with the wall [28]. A_u and A_e can be expressed in terms of the molecular tangential impulse and the energy accommodation coefficients α_u and α_e:

$$A_u = \alpha_u^{-1} - 0.5, \qquad A_e = 2\gamma(\alpha_e^{-1} - 0.5)/(\gamma + 1) \tag{14}$$

In this paper, the accommodation coefficients for LST as well as for the DNS are set to $\alpha_u = \alpha_e = 0.9$, which is taken from Maslov et al. [7] and Koslov et al. [27]. A detailed description of these Knudsen boundary conditions are given in Koslov et al. [27]. A more general form of these conditions can be found in Patterson [29].

It has to be pointed out that these boundary conditions just include the absorptive effect of the porous layer without taking into account any roughness effects of the pores. Nevertheless, the influence of the acoustic absorption on the first modes can also be investigated by this approach.

2. *Southampton SLST Code*

The linear stability code of the University of Southampton can be used for temporal as well as spatial analyses in contrast to the solely spatial treatment in NOLOT. The code solves the linear stability system of equations for the growth of small disturbances superimposed on the prescribed base flow [4].

The results presented here are based on a derivation from the conservative Navier–Stokes equations. The wave functions are the same as described in Eq. (2). If the code is used as a temporal stability solver for comparison with temporal DNS, the wavenumbers α and β are real quantities, and the frequency ω is a complex value. The imaginary part ω_i is the growth rate, which is finally the quantity of interest. A direct matrix solution method is used, with derivatives computed by a mapped Chebyshev method using a minimum of 150 collocation points. The code was validated by comparison with a number of sources in the literature, including Malik [30]. The integrated nonslip boundary-condition formulation for porous walls with cylindrical pores is described in Section II.A.1.

B. Direct Numerical Simulation with FLOWer

For DNS calculations, a high-order variant of the DLR FLOWer code is used. The basic FLOWer code solves the compressible Reynolds-averaged Navier–Stokes equations, written in the conservative form, for a perfect gas flow on block-structured grids with second-order finite-volume techniques and cell-centered or cell vertex variables. The high-order version uses fourth-order central differencing based on implicit compact finite differences in a cell-centered formulation, stabilized by high-order compact filters, applied at the end of each time step [31]. The DNS is initialized by an artificial disturbance at $t = 0$, from which the eigenmode is allowed to develop naturally within the time-accurate calculation. The initial disturbance, which is applied for nonslip as well as for the slip boundary conditions, is an analytical approximation of a second-mode eigenfunction and is expressed as

$$v = 0.0001\exp[-4(y - 0.8)^2]\sin(2\pi x/L_x) \tag{15}$$

The calculations use a periodic boundary condition in the x-direction. A nonslip wall with temperature set to the wall temperature of the base flow is applied at $y = 0$ and on surfaces within pores. At the outer boundary, characteristic conditions are used.

The influence of the Knudsen layer is taken into account as an additional boundary condition. In a first-order approximation, the boundary conditions for a small, finite Knudsen number are

$$\Delta u_w = A_u Kn\left(\frac{\partial u}{\partial r}\right), \qquad \Delta T_w = A_e Kn\left(\frac{\partial T}{\partial r}\right) \tag{16}$$

with Δu_w and ΔT_w as fluid-velocity and temperature jump at the surface, where Δu_w is set as new wall velocity due to the nonslip condition at the bottom of the Knudsen layer, and ΔT_w is added to the adiabatic wall temperature. $\partial u/\partial r$ and $\partial T/\partial r$ are the wall-normal derivatives. The definition of the Knudsen number and the factors A were given in Section II.A.1.

The pores are described as rectangular cavities in a way that the grids match at the interface, removing interpolation as a possible source of error. For this study, the simulations for the DNS were performed in 2-D. Thus, the pores are reduced to spanwise grooves with parallel sides, which are shown in Fig. 1. The given number of pores/grooves in this paper are the number of pores/grooves per wavelength.

C. Introduction of the Gaster Transformation

Because of the fact that the NOLOT LST code is a spatial code, whereas DNS uses a temporal approach for mode-development, a transformation for the comparison of the growth rate is necessary, which is the well-known Gaster transformation [4]:

$$\omega_{i,\text{temporal}} = -\alpha_{i,\text{spatial}} c_{\text{gr}} \tag{17}$$

where ω_i is the temporal growth rate, $-\alpha_i$ is the spatial growth rate, and c_{gr} is the group velocity:

$$c_{\text{gr}} = \frac{\partial\omega_r}{\partial\alpha_r} \tag{18}$$

The Gaster transformation is an approximation that is valid for small growth rates. Within the approximation, the real part of the frequency and the real part of the wave number of the spatial wave are the same as for the temporal wave.

D. Introduction of the Hydraulic Diameter

The hydraulic diameter approach provides a possibility to compare different pore shapes. Different formulations for this quantity will be used. The first formulation, called the hydraulic tube

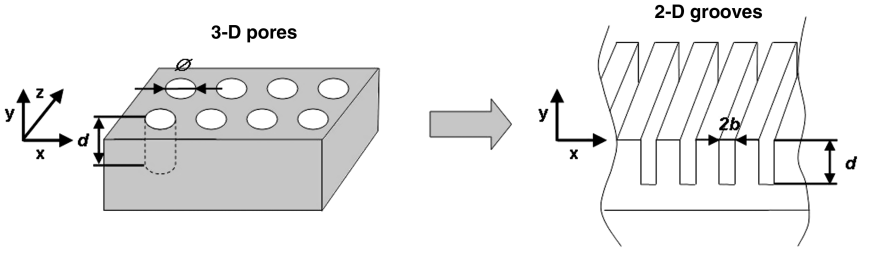

Fig. 1 Pore modeling.

diameter, is a common term to handle flow in noncircular open tubes and channels [32]:

$$d_{h,\text{tube}} = \frac{4A_p}{C} \tag{19}$$

where A_p is, in the present notation, the pore area, and C is the circumference. The second hydraulic diameter, called the hydraulic wetted diameter, comes from the theory of fluid flow through porous, packed beds [33]. The definition of this hydraulic diameter is

$$d_{h,\text{wet}} = \frac{V_p}{S_{\text{wet}}} \tag{20}$$

where V_p is the volume of the pore, and S_{wet} is the wetted surface area, which, for pores, includes the pore bottom. The difference between these two diameters is, essentially, that, for the hydraulic tube diameter, the pore bottom is omitted, whereas it is included in the hydraulic wetted diameter, as demonstrated in the following equations, which show the derivations of the two hydraulic diameters for spanwise grooves with the depth d, width w, and spanwise length a:

$$d_{h,\text{tube,groove}} = \frac{4A_p}{C} = \frac{4wa}{2(a+w)} \overset{a\to\infty}{\to} 2w \tag{21}$$

$$d_{h,\text{wet,groove}} = \frac{V_p}{S_{\text{wet}}} = \frac{wad}{wa + 2wd + 2ad} = \frac{wad}{wad}\frac{1}{(1/d) + [1/(2a)] + [1/(2w)]} \overset{a\to\infty}{\to} \frac{1}{(1/d) + [1/(2w)]} \tag{22}$$

The resulting effect of the diameter differences is shown in the next section.

III. Comparison of Different Pore Shapes by Using Two Different Hydraulic Diameters

This section compares different pore shapes using cylindrical pores and spanwise grooves. In particular, the accuracy of the different definitions of hydraulic diameters is demonstrated. All results in this section are nonslip results.

A. Grids and Flow Conditions

The basic flow parameters of the compressible Blasius flow for the studied porous wall cases and, for completeness, for a smooth wall case are $M_\infty = 6$ at a Reynolds number of $\text{Re} = 2 \times 10^4$, a Prandtl number of $Pr = 0.72$, and a ratio of specific heats ratio of $\gamma = 1.4$. The viscosity μ is prescribed by Sutherland's law with a constant of 110.4 K and a reference temperature of 216.65 K, leading to an adiabatic wall temperature of 1522.44 K.

For the wall-normal grid distribution, a stretching function is used, which places most points near the wall in an analytical way

$$y = L_y \frac{\sinh(c\eta)}{\sinh c} \tag{23}$$

where $\eta_m < \eta < 1$, and c and η_m are chosen iteratively near to a target c such that $y(\eta_m) = -d$, with the pore depth d and an integer number of grid cells within the pore. The pore depth and all coordinates are normalized by the displacement thickness. The DNS calculations of the pores were performed as 2-D spanwise grooves with parallel side walls. The porosity n for all cases is 0.25.

B. LST Results

For the following detailed comparison of both approaches (LST and DNS), the maximum growth rate of the second mode has to be found because the highest damping effect is expected for this value. With the LST, a fast method is provided to calculate the whole spectrum of amplified growth rates, as given in Fig. 2, for a smooth and a porous wall. The SLST code is used here in the temporal mode to provide comparability with the DNS; thus, the temporal growth rate ω_i is plotted as a function of the wave number α for the SLST code (Fig. 2a), whereas, for the spatial NOLOT code, the growth rate in the diagram is $-\alpha_i$ as a function of the real part of the wave number α_r (Fig. 2b). The dashed lines in Fig. 2 show the spectrum for a porous wall with pore depth 1. For this case, the hydraulic tube diameter is 0.09375, corresponding to 16 grooves for the DNS calculation in the following section. The spatial stability diagram shows a maximum growth rate ω_i of 0.003 for the first mode of the smooth wall boundary layer, marked as solid line. Because of the fact that the chosen pores are small enough, the absorption effect on the first mode generates only a slight increase for the porous wall. As expected, the most unstable mode is the second mode, with a maximum spatial growth rate of 0.0453 at a wave number of $\alpha_r = 2.2$. The figure demonstrates the reduction of the second mode amplitude due to the pore effect of absorbing parts of the disturbance energy. With the chosen wall porosity, the maximum growth rate is reduced by 42% in comparison with the smooth wall case for both codes (the temporal SLST code as well as the spatial NOLOT code). By using the Gaster transformation, a maximum temporal growth rate of 0.0372 can be calculated from spatial results. The maximum value predicted by the temporal SLST code is marginally smaller. The relative difference between SLST and NOLOT is less than 0.5%, as shown in Fig. 2.

A direct comparison of NOLOT with the SLST code in spatial mode without using Gaster transformation results in a relative difference of less than 0.05%. These results, including a description of influences of the Navier–Stokes equation formulation in the codes, were given in Wartemann et al. [22].

The dashed line in Fig. 2b shows the LST result without thermal admittance B [see Eq. (4)]. As suggested by Maslov et al. [7], neglecting the thermal admittance is possible without any significant loss of accuracy. The relative difference of the porous wall damping between the results with and without thermal admittance in Fig. 2b has a maximum below 0.5%; thus, the thermal admittance is neglected.

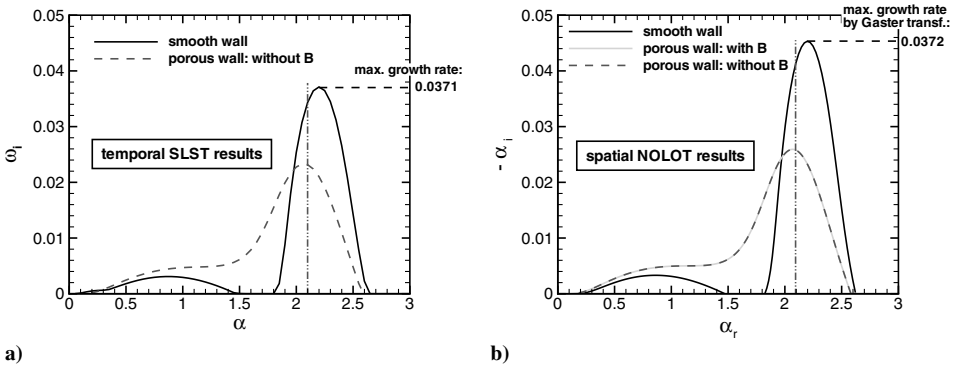

Fig. 2 Stability diagrams calculated by LST, where B is the thermal admittance: a) temporal SLST results and b) spatial NOLOT results.

Another effect, visible in Fig. 2, is a shift in the wave number for the respective cases with and without wall porosity. To keep the following DNS calculations comparable, a fixed wave number α of 2.094, shown by the vertical lines near the second mode maximum, is chosen for all the following test cases.

C. Comparison of DNS with LST Results for Cylindrical Pores by Using the Hydraulic Tube Diameter

The first comparison of DNS with LST data includes 2-D DNS calculations, representing the pores as spanwise grooves with parallel sides. The LST calculations are performed with a boundary condition suitable for cylindrical pores, as defined in Eqs. (8) and (9). Consequently, comparisons are carried out by using the hydraulic diameter. In this section, the hydraulic tube diameter, as defined in Section II.D, is used. The calculations for the DNS are performed for eight and 16 pores per wavelength, which leads to a hydraulic tube diameter of 0.1875 for eight pores and 0.09375 for 16 pores. Also, the pore depth is varied, where the chosen end value for the pore depth depends on the chosen hydraulic diameter (this relation will be explained in the following paragraphs). Figure 3 shows the results of this comparison: Fig. 3a for eight pores and Fig. 3b for 16 pores. In comparison of previously published work by Sandham and Lüdeke [24], an error in the SLST implementation of the porous wall boundary condition has been corrected, with a small improvement in the agreement with DNS results.

In both cases, an oscillatory behavior of the growth rate with the pore depth is visible as well as a limiting value for increasing depth. In the following paragraphs, the pore depth for which the difference of growth rate compares to the limiting value is $\leq 2\%$ is denoted as the depth limit d_l with a corresponding growth rate $\omega_{i,l}$. Both LST results, marked by circles, show very good agreement with each other; hence, LST values are given for only one LST code, which is NOLOT. For the test case with eight pores, the growth rate $\omega_{i,l}$ has a value of 0.0176 at a depth limit of 1.05, and, for 16 pores, the growth rate $\omega_{i,l}$ is 0.0231 at a depth limit of 0.4 taken from LST results. Fedorov et al. [5] described, for a similar test case, that a pore depth of about five diameters calculated by LST is sufficient for an appropriate damping rate, which corresponds well with our results. The approximate depth limit of the growth rates are extracted from Fig. 3 and are listed in Table 1. For comparison with Fedorov et al.'s definition, the third column shows $5d_h$. It can be seen that the values of the depth limits are within the same range. Finally, the percentage growth rates $\omega_{i,l}$ are expressed in Table 1 in relation to the smooth wall case. With an increasing pore diameter, the damping effect becomes stronger, so for eight pores the growth rates are smaller than for 16 pores. The growth rates $\omega_{i,l}$ calculated by DNS and LST show, for both cases, maximum differences below 5%. The trend of the functions in Fig. 3 is identical. The visible deviations at the extreme values of these functions between DNS and LST are attributed to the definition of the hydraulic tube diameter, as shown in the next section.

D. Comparison of DNS and LST by Using a Split Boundary Condition

In this section, the same test cases with eight and 16 pores are investigated, but the 2-D spanwive groove DNS calculations are compared with LST calculations with a boundary condition for grooves instead of cylindrical pores, as defined in Eqs. (10) and (11). Consequently, the comparison (Fig. 4, solid lines) is carried out without using the hydraulic diameter approach. In this section, only LST results from NOLOT are shown. For a better comparison, the LST results from the preceding section (calculated with the hydraulic tube diameter) are illustrated in Fig. 4 by dashed lines, where the temporal growth rate as a function of the pore depth is shown. In both cases, a better agreement between LST and DNS is visible by using the groove shape for the LST boundary condition instead of the cylindrical pore approach in combination with the hydraulic tube diameter, particularly at the extrema. For example, for a pore depth of 0.3 with eight pores, the relative difference between DNS and LST is reduced from about 23% down to 1%. For the growth rates $\omega_{i,l}$, an even better agreement is reached. The relative difference in both cases is below 2%, which is a good agreement for the two completely different approaches.

E. Comparison of DNS with LST Results for Cylindrical Pores by Using the Hydraulic Wetted Diameter

Because of the differences between DNS and LST resulting from the use of the hydraulic tube diameter (see Fig. 4), another definition of the hydraulic diameter is investigated to compare different pore shapes. The same test cases with eight pores are investigated, but, now, the LST calculations with a cylindrical pore boundary condition use the hydraulic wetted diameter from Eq. (20) (instead of the hydraulic tube diameter) for comparisons with 2-D DNS. In Fig. 5, DNS results are marked as square symbols and LST by circles. For a better comparison, the LST calculations using the hydraulic tube diameter are shown by a dashed line. It is clear that differences at the

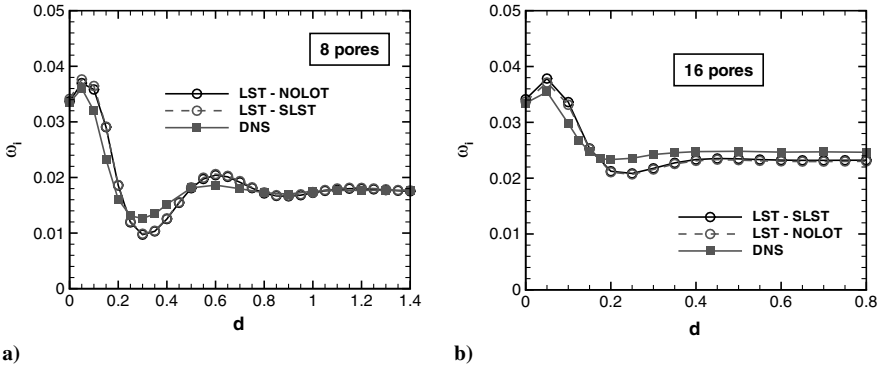

a) b)

Fig. 3 Variation of the pore depth; comparison of DNS with LST by hydraulic tube diameter: a) eight pores and b) 16 pores.

Table 1 Comparison of DNS with LST by hydraulic tube diameter

Number of pores	Method	Five pore diameters	Limit-pore depth	Limit-growth rate	Limit-growth rate
n_p	-	$5d_h$	d_l	$\omega_{i,l}$	$\omega_{i,l}$, % of smooth wall case
8	DNS	0.93750	1.00	0.0175	52.4%
8	LST	0.93750	1.05	0.0176	52.2%
16	DNS	0.46875	0.35	0.0245	73.4%
16	LST	0.46875	0.40	0.0231	68.5%

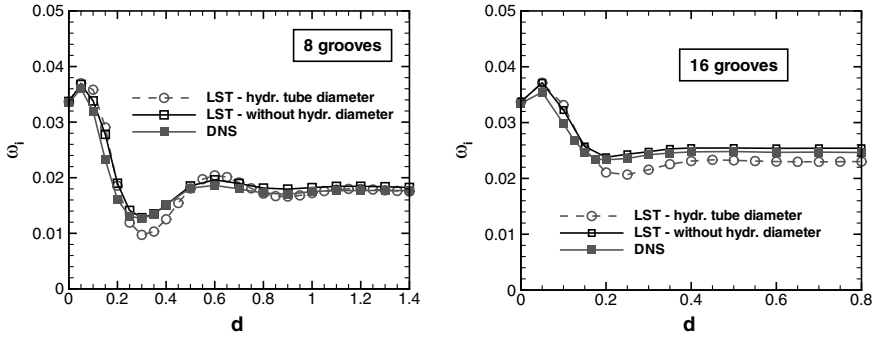

a) b)

Fig. 4 Variation of the groove depth; comparison of DNS with LST without using hydraulic tube diameter: a) eight grooves and b) 16 grooves.

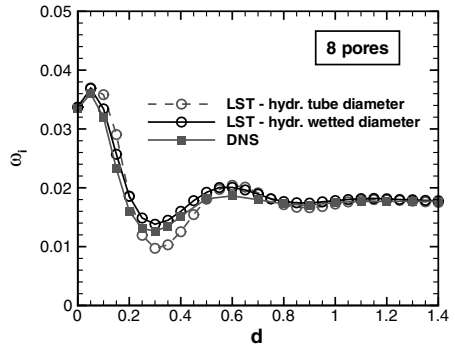

Fig. 5 Variation of the pore depth; comparison of DNS with LST using two different defined hydraulic diameters: eight pores.

extrema are significantly reduced by using the new formulation. One reason for the better agreement is the appearance of the pore depth in the formulation of the hydraulic wetted diameter, whereas, for the hydraulic tube diameter, no pore depth appears [see Eqs. (21) and (22)]. As a concluding remark, the hydraulic wetted diameter supplies reasonable results for all cases, whereas the hydraulic tube diameter is only a good approach for deep pores.

IV. Slip Boundary Condition

In this section, the necessity of a slip boundary condition is investigated. Two-dimensional DNS calculations are compared with LST results, calculated by a spanwise groove boundary condition. The freestream conditions, chosen wave numbers, and grids are all the same as in preceding sections. For the first detailed comparison (Sections IV.A and IV.B), two different Knudsen numbers of 0.1 and 0.2 were chosen, deliberately selected from planned wind tunnel conditions of tests at DLR facilities, using cones with porous surfaces. The wind tunnel conditions corresponding to flight altitudes between 28 km to 33 km, where the Knudsen number calculated by Eq. (13) ($Kn = 4\mu/(\rho \bar{c} b)$) is less than 0.1, used the planned pore diameter for the experiments as reference length b. For the first case (Section IV.A) the artificial Knudsen number is set to 0.2. The groove half-width b is 0.0234375, corresponding to 16 grooves for the DNS, and a groove depth d of 1.0 is chosen. The groove half-width of the second case (Section IV.B) is, with 0.046875, twice as large as that of the first test case and corresponds to eight grooves for the DNS. To provide consistency in the Knudsen number for both pore widths, for the second case, with a doubled width, the Knudsen number is reduced to 0.1 [see Eq. (13)]. For this case, a groove depth of 1.5 is chosen. The selected depths are in the range of the respective depth limit (see Fig. 4). An overview of the simulated test cases of Sections IV.A and IV.B, including the smooth wall case with $d = 0$, is shown in Table 2. In Section IV.C, the influence of the groove depth for eight grooves and a Knudsen number of 0.1 is shown. In Section IV.D, the Knudsen number is varied from 0 to 0.4 for eight and 16 grooves. For the purposes of this study, the Knudsen number is varied independently of the groove width.

Table 2 Overview of test cases with finite Knudsen number of Sections IV.A and IV.B

	Boundary condition	Number of grooves	Groove half-width b	Groove depth d
Smooth wall	-	0	0	0
Porous wall	Nonslip	16	0.0234375	1.0
Porous wall	Slip at $Kn = 0.2$	16	0.0234375	1.0
Porous wall	Nonslip	8	0.0468750	1.5
Porous wall	Slip at $Kn = 0.1$	8	0.0468750	1.5

A. Test Cases with 16 Grooves at $Kn = 0.2$

In this subsection, a detailed overview of the test cases with 16 grooves at a Knudsen number of 0.2 and a groove depth of 1 is given.

1. *Mack Mode Development: DNS Results*

Figure 6 shows wall-normal velocity contours from DNS for Mack modes developing on a smooth surface in comparison with porous surfaces. In Fig. 6a, the normal velocity in a boundary layer over a smooth wall is plotted, whereas Figs. 6b and 6c demonstrate the reduction of the Mack mode amplitude at the same time. As is visible by comparing the legends of the figures, the values with grooves are smaller. For the case with a slip boundary condition at $Kn = 0.2$ (right), an additional reduction is visible by comparing the maximum vales in the legends with the nonslip boundary condition (middle). The flow over the grooves using the slip boundary condition is comparable with a nonslip boundary condition with an increased diameter. This behavior results from a finite velocity at the pore walls for nonzero Knudsen numbers, generating a velocity profile in the pore cross section equivalent with those of larger tubes but nonslip walls. So, practically, the grooves are widened for the instabilities, which results in an increasing damping effect, taking the Knudsen number into account, as described by Maslov et al. [7].

2. *Comparison of Eigenfunctions from LST and DNS*

As already pointed out, both codes provide essentially different approaches, so the comparability of the eigenfunctions has to be shown explicitly. This is done in Fig. 7 for smooth wall (Fig. 7a), porous surface (Fig. 7b), and the additional consideration of the Knudsen layer (Fig. 7c). The eigenfunctions compare well, though for the slip boundary condition in Fig. 7c, differences in the second maximum are visible.

3. *Comparison of LST with DNS: Growth Rates*

Figure 8 shows the development of the natural logarithm of the root mean square v perturbation, integrated in the y-direction. As the DNS simulation proceeds over a number of time steps, the unstable mode has emerged from the rough initial approximation and grows strongly over the remainder of the simulation. The growth rates are extracted from the slopes of the lines. In all cases, DNS predicts

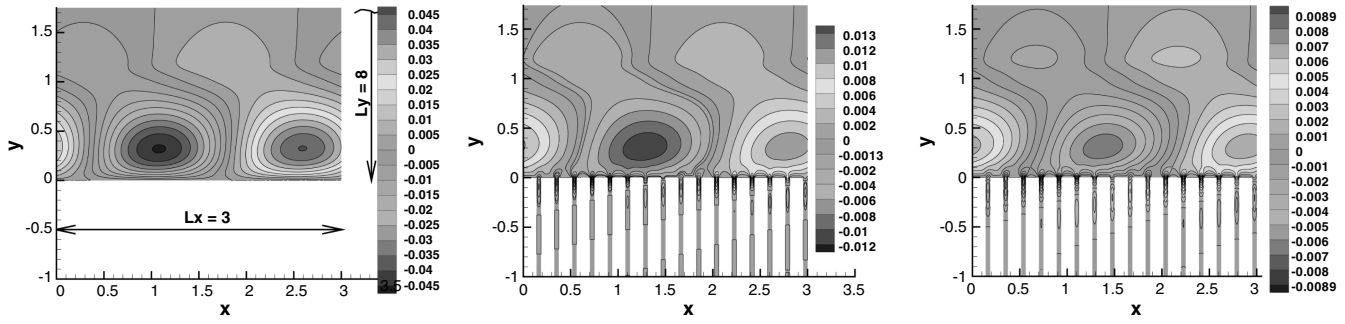

Fig. 6 DNS (contours of v): a) Mack mode developing above a smooth wall, b) a porous surface with nonslip boundary condition, and c) slip boundary condition at $Kn = 0.2$ at the same time.

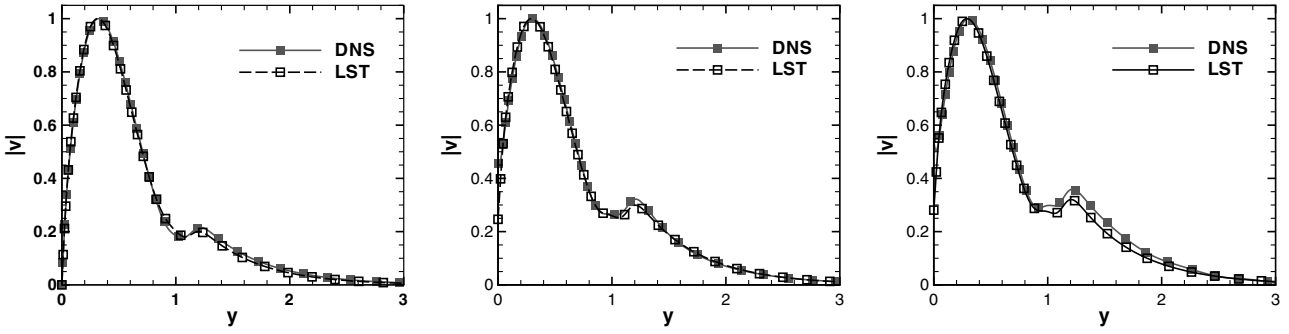

Fig. 7 Comparison of the amplitude functions (16 grooves) groove depth $d = 1.0$: a) smooth wall, b) porous surface with nonslip boundary condition, and c) slip boundary condition at $Kn = 0.2$.

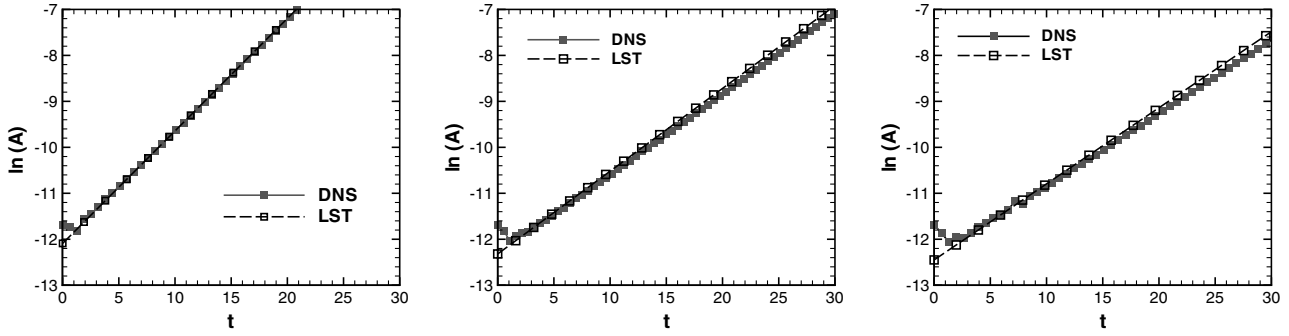

Fig. 8 DNS values of disturbance amplitude and LST growth rates for 16 grooves (groove depth $d = 1.0$): a) smooth wall, b) porous surface with nonslip boundary condition, and (c) slip boundary condition at $Kn = 0.2$.

slightly lower growth rates than LST and, thus, a higher damping. For a better comparison of the damping, Table 3 shows the percentage values related to the growth rate of the smooth wall case and to the porous wall case with a nonslip boundary condition. A significant additional damping effect, resulting from the modeling of the Knudsen layer, is visible for both prediction methods; the damping, expressed in relation to the porous wall with a nonslip boundary condition, is 9.1% for the DNS and 8.3% for the LST calculations.

B. Test Cases with Eight Grooves at $Kn = 0.1$

The next test cases are performed with eight grooves, resulting in a doubled half-width compared with the former ones with 16 grooves, and a groove depth of 1.5. For this case, the Knudsen number was reduced to 0.1, half the size of the previous 16 groove geometry ($Kn = 4\mu/(\rho\bar{c}b)$).

The amplitude growth rates are illustrated in Fig. 9, including the smooth wall case from Fig. 9 for a better visual comparison of the slope. For the same reason, the previous test cases are added in light gray in the diagrams. As in the previous test cases, the predicted

Table 3 Comparison of the damping effect for 16 grooves and groove depth $d = 1.0$

	Boundary condition	ω_i, % of smooth wall case	ω_i, % of porous nonslip wall case
DNS	Nonslip	74.0	-
LST	Nonslip	75.4	-
DNS	Slip $Kn = 0.2$	67.2	90.9
LST	Slip $Kn = 0.2$	69.1	91.7

Table 4 Comparison of the damping effect for eight grooves and groove depth $d = 1.5$

	Boundary condition	ω_i, % of smooth wall case	ω_i, % of porous nonslip wall case
DNS	Nonslip	52.9	-
LST	Nonslip	54.4	-
DNS	Slip $Kn = 0.1$	50.4	95.3
LST	Slip $Kn = 0.1$	52.4	96.4

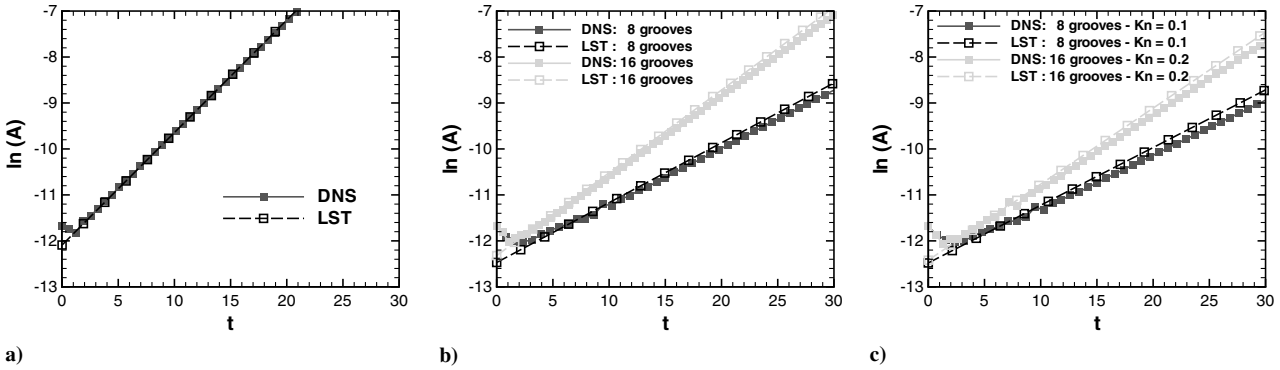

Fig. 9 DNS values of disturbance amplitude and LST growth rates: a) smooth wall, b) porous surface with nonslip boundary condition, and (c) slip boundary condition at different Knudsen numbers.

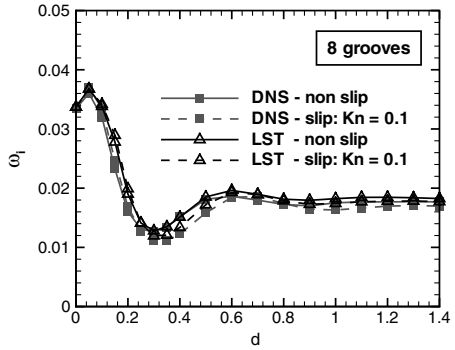

Fig. 10 Variation of the groove depth (eight grooves); comparison of nonslip/slip boundary conditions.

growth rates are slightly larger for LST than for DNS calculations. Because of the larger diameter, the damping effect is larger for eight grooves than for 16 (compare Tables 3 and 4). The additional damping effect of the slip boundary condition is naturally lower for the smaller Knudsen number but still visible for both prediction methods.

C. Influence of the Groove Depth

For comparison of the nonslip boundary condition with the slip condition, a detailed study of the influence of the groove depth is carried out, including the same eight groove test cases. The result in Fig. 10 shows the growth rate as a function of the groove depth for eight grooves.

By modeling the Knudsen layer, the groove depth has a stronger effect for all cases because of the effectively larger groove width, as already described. With the effectively widened grooves, the transient oscillation behavior, which is visible, for example, in the shifts of the first minima and second maxima, changes and, consequently, the limit-groove depth increases, as already described. Here, the limit-groove depth is increased from 1.0 to 1.1 for LST as well as for DNS.

D. Examination of the Impact of Slip Boundary Conditions

In addition to the verification of the slip boundary condition in both codes, it is necessary to investigate the physical impact of the slip boundary condition at different Knudsen numbers. Thus, in this section, the Knudsen number is varied between 0 to 0.4 for both previous test cases with eight grooves and 16 grooves. For the purposes of this study, the Knudsen number is varied independently of the groove width. This is equivalent to using a fixed reference length other than the groove width in Eq. (13); otherwise, there would be an inconsistency when cases with a different number of grooves are used per wavelength of the instability. A fixed groove depth is set with 1.5 for eight grooves and 1.0 for the 16 groove cases, so the limit-groove depth is reached for all cases, as shown in the preceding section.

Figure 11 shows the growth rate as a function of the Knudsen number (Fig. 11a for eight grooves and Fig. 11b for 16 grooves). Results from the smooth test cases are included in the diagram for a better appraisement of the Knudsen number effect. In both diagrams, an additional damping effect is visible, which is stronger for 16 grooves than for eight grooves. If linear functions are used to fit the averaged gradients, the slope of the function for 16 grooves from LST is around twice as large as for eight grooves. The reason for this behavior is found by the initial damping of the grooves; with 16 grooves, the initial damping effect expressed in relation to the smooth wall case without rarefied gas influences is 75.4% (LST), whereas, for eight grooves, the initial damping effect is about 54.4% (LST). As a result, the additional damping of slip boundary conditions depends strongly on the initial growth rate calculated by nonslip conditions. For test cases with a low damping effect of the grooves and, thus, with high initial growth rates, the effect of the Knudsen number on the result is found to be significant.

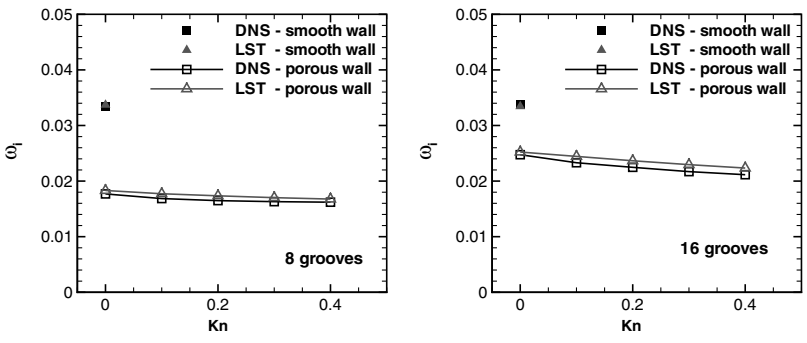

Fig. 11 Variation of the Knudsen number: a) eight grooves and b) 16 grooves.

V. Conclusions

In the present study, a second-mode stability analysis was performed for a boundary layer flow at Mach 6 over different porous walls. Two different approaches were compared successfully; DNS, by a fourth-order finite difference code, which is used to provide complete solutions, including the flow inside pores, was compared with two different linear stability codes: the spatial NOLOT code and the spatial/temporal SLST code. The trends of the predicted functions for both methods are identical; the limit-pore depths are nearly the same, and the small differences for the predicted growth rate $\omega_{i,l}$ are less than 2%. The investigation shows influences of pore shape (cylindrical pores and spanwise grooves). In particular, two different hydraulic diameters are defined, and their applicability on the present cases was investigated. It has been shown that the hydraulic tube diameter approach can be used with good results only for deep pores, particularly after reaching the defined limit-pore depth. In case of pore depth below the limit-pore depth, differences over 20% are possible. The hydraulic wetted diameter, on the other hand, shows improved accuracy for all pore depths.

Additionally, the influence of the Knudsen boundary condition was investigated for different pore diameters, depths, and Knudsen numbers. The investigation of the slip boundary condition shows, for all cases, an additional damping effect compared with the nonslip approach, resulting from an effective increase of the pore diameter. For test cases with a low damping effect of the pores and, thus, with larger growth rates, the impact of the Knudsen number on the result is found to be significant.

Acknowledgments

The presented results are partly performed in the framework of the Integrated Multidisciplinary Design of Hot Structures (IMENS-3C) project. The authors would like to acknowledge the support of the IMENS-3C project management.

References

[1] Schneider, S., "Flight Data for Boundary Layer Transition at Hypersonic and Supersonic Speeds," *Journal of Spacecraft and Rockets*, Vol. 36, No. 1, 1999, pp. 8–20. doi:10.2514/2.3428

[2] Schneider, S., "Hypersonic Laminar-Turbulent Transition on Circular Cones and Scramjets Forebodies," *Progress in Aerospace Sciences*, Vol. 40, Nos. 1–2, 2004, pp. 1–50. doi:10.1016/j.paerosci.2003.11.001

[3] Joslin, R., "Overview of Laminar Flow Control," NASA, TB 1998-208705, 1998.

[4] Mack, L. M., "Boundary Layer Linear Stability Theory," *AGARD Special Course on Stability and Transition of Laminar Flow*, AGARD, 1984.

[5] Fedorov, A. V., Malmuth, N. D., Rasheed, A., and Hornung, H. G., "Stabilization of Hypersonic Boundary Layers by Porous Coatings," *AIAA Journal*, Vol. 39, No. 4, 2001, pp. 605–610. doi:10.2514/2.1382

[6] Rasheed, A., Hornung, H. G., Fedorov, A. V., and Malmuth, N. D., "Experiments on Passive Hypervelocity Boundary-Layer Control Using an Ultrasonically Absorptive Surface," *AIAA Journal*, Vol. 40, No. 3, 2002, pp. 481–489. doi:10.2514/2.1671

[7] Maslov, A., Fedorov, A. V., Kozlov, V. F., Mironov, S. G., Shiplyuk, A. N., Tsyrulnikov, I. S., Burov, E. V., and Sapogov, B., "Experimental and Theoretical Studies of Hypersonic Laminar Flow Control Using Ultrasonically Absorptive Coatings (UAC)," ISTC, Rept. 2172-2001, May 2003.

[8] Fedorov, A., Shiplyuk, A., Maslov, A., Burov, E., and Malmuth, N., "Stabilization of a Hypersonic Boundary Layer Using an Ultrasonically Absorptive Coating," *Journal of Fluid Mechanics*, Vol. 479, 2003, pp. 99–124. doi:10.1017/S0022112002003440

[9] Fedorov, A., Kozlov, V., Shiplyuk, A., Maslov, A., Sidorenko, A., Burov, E., and Malmuth, N., "Stability of Hypersonic Boundary Layer on Porous Wall with Regular Microstructure," *33rd AIAA Fluid Dynamics Conference and Exhibit*, AIAA Paper 2003-4147, Orlando, FL, June 2003.

[10] Kozlov, V., Fedorov, A., and Malmuth, N., "Acoustic Properties of Rarefied Gases Inside Pores of Simple Geometries," *Journal of the Acoustical Society of America*, Vol. 117, No. 6, June 2005, pp. 3402–3412. doi:10.1121/1.1893428

[11] Chokani, N., Bountin, D., Shiplyuk, A., and Maslov, A., "Nonlinear Aspects of Hypersonic Boundary Layer Stability on a Porous Surface," *AIAA Journal*, Vol. 43, No. 1, Jan. 2005, pp. 149–155. doi:10.2514/1.9547

[12] Fedorov, A., Shiplyuk, A., Maslov, A., Kozlov, V., Sidorenko, A., and Malmuth, N., "Hypersonic Laminar Flow Control Using a Porous Coating of Random Microstructure," *44th AIAA Aerospace Sciences Meeting and Exhibit*, AIAA Paper 2006-1112, Reno, NV, Jan. 2006.

[13] Maslov, A., Fedorov, A., Bountin, D., Shiplyuk, A., and Sidorenko, A., "Experimental Study of Transition in Hypersonic Boundary Layer on Ultrasonically Absorptive Coating with Random Porosity," *46th AIAA Aerospace Sciences Meeting and Exhibit*, AIAA Paper 2008-587, Reno, NV, 7–10 Jan. 2008.

[14] Fedorov, A., and Malmuth, N., "Parametric Studies of Hypersonic Laminar Flow Control Using a Porous Coating of Regular Microstructure," *46th AIAA Aerospace Sciences Meeting and Exhibit*, AIAA Paper 2008-588, Reno, NV, 7–10 Jan. 2008.

[15] Fedorov, A., Kozlov, V., and Addison, R., "Reflections of Acoustic Disturbances from a Porous Coating of Regular Microstructure," *5th AIAA Theoretical Fluid Mechanics Conference*, AIAA Paper 2008-3902, Seattle, WA, 23–26 June 2008.

[16] Fedorov, A., "Temporal Stability of Hypersonic Boundary Layer on Porous Wall: Comparison of Theory with Direct Numerical Simulation," *48th AIAA Aerospace Sciences Meeting Including the New Horizons Forum and Aerospace Exposition*, AIAA Paper 2010-1242, Orlando, FL, 4–7 Jan. 2010.

[17] Egorov, I. V., Fedorov, A. V., Novikov, A. V., and Soudakov, V. G., "Direct Numerical Simulation of Supersonic Boundary-Layer Stabilization by Porous Coating," *45th AIAA Aerospace Sciences Meeting and Exhibit*, AIAA Paper 2007-948, Reno, NV, 2007.

[18] Bres, G. A., Colonius, T., and Fedorov, A. V., "Interaction of Acoustic Disturbances with Micro-Cavities for Ultrasonic Absorptive Coatings," *5th AIAA Theoretical Fluid Mechanics Conference*, AIAA Paper 2008-3903, Seattle, WA, 23–26 June 2008.

[19] Bres, G. A., Colonius, T., and Fedorov, A. V., "Stability of Temporally-Evolving Supersonic Boundary Layers over Micro-Cavities for Ultrasonic Absorptive Coatings," *5th AIAA Theoretical Fluid Mechanics Conference*, AIAA Paper 2008-4337, Seattle, WA, 23–26 June 2008.

[20] Bres, G. A., Inkman, M., Colonius, T., and Fedorov, A. V., "Alternate Design of Ultrasonic Absorptive Coatings for Hypersonic Boundary Layer Control," *39th AIAA Fluid Dynamics Conference*, AIAA Paper 2009-4217, San Antonio, TX, 22–25 June 2009.

[21] Lüdeke, H., Wartemann, V., and Sandham, N. D., "Numerical Investigation of Transition Control by Porous Surfaces in Hypersonic Boundary Layers," *New Results in Numerical and Experimental Fluid Mechanics VII*, edited by A. Dillmann, G. Heller, M. Klaas, H.-P. Kreplin, W. Nitsche, and Schröder, W., Vol. 112, Notes on Numerical Fluid Mechanics and Multidisciplinary Design (NNFM), Springer–Verlag, Berlin/New York/Heidelberg, 2010.

[22] Wartemann, V., Lüdeke, H., and Sandham, N. D., "Stability Analysis of Hypersonic Boundary Layer Flow Over Microporous Surfaces," *16th AIAA/DLR/DGLR International Space Planes and Hypersonic Systems and Technologies Conference*, AIAA Paper 2009-7202, Bremen, Germany, 19–22 Oct. 2009.

[23] Wartemann, V., and Lüdeke, H., "Investigation of Slip Boundary Conditions of Hypersonic Flow Over Microporous Surfaces," *Fifth European Conference on Computational Fluid Dynamics*, ECCOMAS 01073, Lisbon, Portugal, 14–17 June 2010.

[24] Sandham, N. D., and Lüdeke, H., "A Numerical Study of Mach 6 Boundary Layer Stabilization by Means of a Porous Surface," *AIAA Journal*, Vol. 47. No. 9, Sept. 2009, pp. 2243–2252. doi:10.2514/1.43388

[25] De Tullio, N., and Sandham, N. D., "Direct Numerical Simulation of Breakdown to Turbulence in a Mach 6 Boundary Layer Over a Porous Surface," *Physics of Fluids*, Vol. 22, No. 9, 2010, p. 094105. doi:10.1063/1.3481147

[26] Hein, S., Bertolotti, F. P., Simen, M., Hanifi, A., and Henningson, D., "Linear Nonlocal Instability Analysis: The Linear NOLOT Code," DLRIB 223-94 A56, 1994.

[27] Koslov, V. F., Fedorov, A. V., and Malmuth, N. D., "Acoustic Properties of Rarefied Gases Inside Pores of Simple Geometries," *Journal of the Acoustical Society of America*, Vol. 117, No. 6, June 2005, pp. 3402–3412. doi:10.1121/1.1893428

[28] Godman, F. O., and Wachman, H. Y., *Dynamics of Gas-Surface Scattering*, Academic Press, New York/London/Orlando, FL, 1976.
[29] Patterson, G. N., *Molecular Flow of Gases*, Wiley, New York, 1956.
[30] Malik, M. R., "Numerical Methods for Hypersonic Boundary Layer Stability," *Journal of Computational Physics*, Vol. 86, No. 2, 1990, pp. 376–413.
doi:10.1016/0021-9991(90)90106-B
[31] Enk, S., "Ein Verfahren Höherer Ordnung in FLOWer für LES,"DLR, IB 124-2007/8, 2007.
[32] Allard, J. F., and Atalla, N., *Propagation of Sound in Porous Media*, 2nd ed., Wiley, New York, 2009.
[33] Blake, F. C., "The Resistance of Packing to Fluid Flow," *Transactions of American Institute of Chemical Engineers*, Vol. 14, 1922, pp. 415–421.

X. Zhong
Associate Editor